

Received July 31, 2021, accepted August 11, 2021, date of publication August 16, 2021, date of current version August 25, 2021.

Digital Object Identifier 10.1109/ACCESS.2021.3105390

Seat-Occupancy Detection System and Breathing Rate Monitoring Based on a Low-Cost mm-Wave Radar at 60 GHz

ANTONIO LAZARO^{id}, (Senior Member, IEEE), MARC LAZARO^{id}, RAMON VILLARINO^{id}, AND DAVID GIRBAU^{id}, (Senior Member, IEEE)

Electronics, Electrical and Automatics Engineering Department, Universitat Rovira i Virgili, 43007 Tarragona, Spain

Corresponding author: Antonio Lazaro (antonioramon.lazaro@urv.cat)

This work was supported in part by under Grant PRE2019-089028, in part by the Spanish Government under Project RTI2018-096019-B-C31 and Project R2B2020/02, and in part by the European Union's European Regional Development Fund (ERDF).

ABSTRACT This work presents a seat-occupancy detection system based on a PCR (Pulsed Coherent Radar) at the unlicensed 60 GHz ISM band. The radar can measure distances with sub-millimeter resolution. Therefore, the system can detect the presence of people occupying the seats by measuring small movements of the body, such as those produced by breathing. In consequence, the system not only measures seat-occupancy but also breathing rate, which is estimated from the amplitude peaks after filtering the amplitude measured by the radar to remove the noise. The effect of the car vibrations and random body movement is experimentally studied. Measurements performed with adults, as well as with a baby emulator sitting in a child seat, are presented. Comparison of the system with another that measures the breath based on airflow shows good agreement and permits its validation.

INDEX TERMS Automotive radar, mm-wave radar, seat occupancy, detection, vital-sign monitoring, breathing monitoring.

I. INTRODUCTION

Vehicle Seat-occupancy detection systems have taken on importance with the introduction of the airbag system. Airbag systems are fundamental safety elements in vehicles but, for proper operation, they require information about the presence and type of occupant of the seat. Undesired activation of the airbag results in a high repair cost. In addition, an airbag deployment in a seat occupied by an infant sitting in a rear-facing baby seat can cause fatal injuries [1]. Therefore, sensors capable of detecting seat occupancy are required, inhibiting the activation of the airbag when the seat is occupied [2]. The seat occupancy detector can also be used as a seat belt reminder. Conventional seat belt reminder systems work with weight sensors. Therefore, they produce undesired alarms when the seats are occupied by luggage or purchases. In addition to meeting regulatory requirements, seat occupancy detection systems can also be used to improve passenger comfort, for example, controlling the air conditioning system according to the occupancy rate. Another

application is to warn of the presence of children or pets. This prevents the driver from accidentally forgetting them inside the car. Besides, one of the most effective ways to reduce pollution in the cities is to promote the reduction of vehicle traffic, encouraging the vehicle sharing. In the same line, on some highways, discounts are applied to vehicles with high occupancy. In addition, tracking drivers' vital signs can alert drivers to stress [3], apnea [4]–[6] or drowsiness [7], which can increase the likelihood of traffic accidents. In consequence, radar-based seat occupancy detection has two main benefits. First of all, it is able to detect occupation avoiding both the contact with the passenger as well as the installation of any auxiliary equipment in the seat and, second, thanks to the measurement of vital signs (such as breathing rate), it is possible to distinguish objects from living beings and to track the conditions of drivers. However, the signal received by the radar will not only contain information about the passenger's vital signs, but also about the voluntary passenger's movements and about those induced by the motion of the car. Consequently, monitoring vital signs using a radar-based sensor becomes quite difficult in a non-stationary environment. An accelerometer can be used to acquire information about

The associate editor coordinating the review of this manuscript and approving it for publication was Shadi Alawneh^{id}.

the unwanted motion induced by the car in order to cancel it. Reference [8]. The main contribution of this paper is to study the feasibility of using a low-cost pulsed mm-Wave radar to implement a seat occupancy detection system and to monitor the driver's breathing rate. The pulsed radar operates in the 60 GHz band. Millimetre-wave transmission in the 60 GHz range is seen to be a promising method to meet the demanding requirements of future wireless systems with regard to increasing data rates. The main advantages of this frequency band are the large (license-free) bandwidth that allows high data rates and the short wavelength is suitable for indoor applications using small antennas. The advantage of this radar compared to other mm-wave Frequency-Modulated Continuous-Wave (FMCW) radars is the integrated system-on-chip solution characterized by high accuracy in distance measurements, without requiring the use for complex signal processing units. Therefore, the system can be implemented using low-power microcontrollers. Also, there is no interference with existing radio systems because most of the communication systems operate at lower frequencies, and specifically automotive radars in the 24 GHz and 77 GHz bands.

The rest of the paper is organized as follows. Section II revises different non-contact seat occupancy detectors, especially based on a radar. Section III describes the proposed solution. Experimental results are given in section IV. Finally, conclusions are provided in section V.

II. RELATED WORKS

Different methods for seat occupancy detection have been proposed in the literature. These can be classified as contact and non-contact methods. The first method is characterized by the installation of a wired sensor in the seat that detects the presence of an occupant, whereas the second method is based on devices that sense the presence at a certain distance using electromagnetic waves or optical systems. Table 1 summarizes several seat occupancy devices reported in the literature, including both the method used for measurement and some additional comments. In the first method, we can find pressure sensors [9], [10]. The main problem of these sensors is their sensitivity to vibration and the requirement of body contact with the seat. Breathing measurements with piezoelectric sensors integrated into the seating area are difficult. It can also be activated when objects are placed on the seat. Another group of sensors is based on capacitive detection, which work on electrode arrays integrated into the seat [11]–[13]. This method is used in ECG measurements [13]. However, these sensors are sensitive to both interference and to the distance between the body and the seat.

Seat-occupancy detection using optical sensors could be an alternative to the current detection methods, especially for rear seats. An example of this is a method based on a camera. The main drawback is that it relies on face or shape detection, making it difficult to work under low light conditions or when children are covered with a clothing. Thanks to body heat, infrared cameras can detect people in low light conditions, but

humans cannot be detected when the inside of the car is hot, as normally happens in summer. Besides, infrared cameras are more expensive than conventional cameras. These vision systems require advanced signal processing algorithms with a high computational cost that contribute to increase the cost of the system. Time-of-Flight LIDAR sensors have also been proposed for seat detection [14]. Recently, a camera-based method for measuring breathing has been proposed in [15]. It is based on the detection of a reflective object attached to the belt.

Vital-signs monitoring has been studied in the literature using different radars such as Impulse Radio Ultra-Wide Band (IR-UWB) [16]–[19], Continuous Wave (CW) Doppler radar [20]–[23] and Frequency-Modulated Continuous-Wave Radar (FMCW) Radar [24], [25]. Vital signs using millimeter wave radar, specially based on Doppler radar, exploits the ability of detection of microdoppler phase shift induced by the chest and heart movements [26], [27]. A fully integrated CMOS Doppler radar has been designed for this application in [28]. In addition to the microdoppler signature detection, FMCW radars can also determine the range [29] of multiple persons and even the angle using beamforming techniques with a multichannel front-end [30]. However, these radars have a higher complexity and require higher computational efforts than simple CW radars or the proposed pulse coherent radar used in this work. Despite this interest, the application of vital-signs monitoring to automotive environments is restricted to a relatively small number of works [31]–[33]. Seat occupancy based on FMCW microwave and mm-wave radars at 24 GHz and 77 GHz have been recently proposed in [34] and [35], respectively. Seat occupancy detection based on monitoring the received UWB signal has been proposed in [36]. A system based on channel measurements from mmWave WiFi devices (60-GHz 802.11ad devices) was recently proposed in [37] for human activity monitoring at room-level. The system uses signal-to-noise ratio (SNR) and channel state information (CSI) measurements, with a classification method for human pose recognition and seat occupancy sensing. Besides vital-sign monitoring, novel mmWave radar applications for object and material classification have recently been proposed [38]–[40].

III. SYSTEM DESIGN AND THEORETICAL BACKGROUND

A. PULSED RADAR OPERATION

A mmWave radar from Acconeer is used in this work. Acconeer's radar is based on PCR (Pulsed Coherent Radar) technology that operates at the unlicensed 60 GHz band. This makes possible to use a very small antenna and ultra-short pulses. The core is an A111 radar sensor [44] that is a System-in-Package (SiP): it integrates the mm-Wave front-end, antenna, memory, logic control and digitization of received signal in one chip. This solution makes it possible to identify materials and detect motion in advanced sensor applications. The radar is characterized for its millimeter accuracy in range and low power consumption. It can measure ranges between 60 - 2000 mm for a RCS of -21 dBsm

TABLE 1. Seat occupancy detectors.

Ref.	Sensor	Wireless	Comments
[9]	Pressure	No	Pressure map from 42x48 pressure sensor matrix
[10]	Pressure	No	Weight measuring system integrated in the seat
[12]	Capacitive	No	Electrodes installed inside the seat
[13]	Capacitive	No	capacitive electrocardiogram (cECG) monitoring, mechanical movement analysis (ballistocardiogram, BCG)
[11]	Capacitive	No	Seat detection based on capacitive sensor integrated in the seats
[41]	Magnetic switch	No	Occupant and infant seat detection
[42]	Stereovision	Yes	Detection and classification of passenger seat occupancy using stereovision
[43]	Camera	Yes	Face detection
[15]	Camera	Yes	Breathing measurement but requires illumination
[14]	Optical sensor	Yes	3D-optical time-of-flight (TOF) sensor
[34]	FMCW	Yes	Rear seat detection based on AoA
[35]	FMCW	Yes	FMCW AoA and SVM classification
[36]	UWB	Yes	CIR variations due to human movements and learning machine algorithms
[37]	mm Wave WiFi	Yes	Propagation channel variations due to human movements and learning machine algorithms

(sphere of radius $r = 50$ mm), having a continuous sweep update frequency configurable up to 1500 Hz. The Half Power Beam Width (HPBW) is 40 and 80 degrees in E-plane and H-plane, respectively. The radar is available in a commercial module (XM132) ready for evaluation and integration and its cost is around 16 €.

Figure 1 shows schematically the waveform transmitted by the pulsed radar. It is a modulated wavelet at the carrier frequency ($f_c = 60$ GHz). The interval between pulses is determined by the PRF that is equal to 13 MHz. The duration of the wavelet (T_{PULSE}) can be configured between a set of five values. The transmitter effective isotropic radiated power (EIRP) is 10 dBm. The typical range resolution is on the order of 0.5 mm. The leakage between the transmitter and the receiver limits the minimum detection distance to about 6 cm for the minimum pulse length. The system relies on the transmission of coherent phase pulses. Therefore, the received signals from multiple pulses are combined to improve the signal-to-noise ratio (SNR), thus enhancing the visibility of the object.

Transmitted signals bounce off in an object. The distance to the object (r) is calculated from the time elapsed between transmission and reception of the reflected signal (τ):

$$r = \frac{c\tau}{2} \tag{1}$$

where c is the propagation velocity.

The radar is installed in front of the seat. The transmitted signal $x_r(\tau)$ can be expressed as a train of wavelets modulated by the carrier frequency:

$$x_r(\tau) = \sum_{k=0}^N p(\tau - kT) \cos(2\pi f_c(\tau - kT)) \tag{2}$$

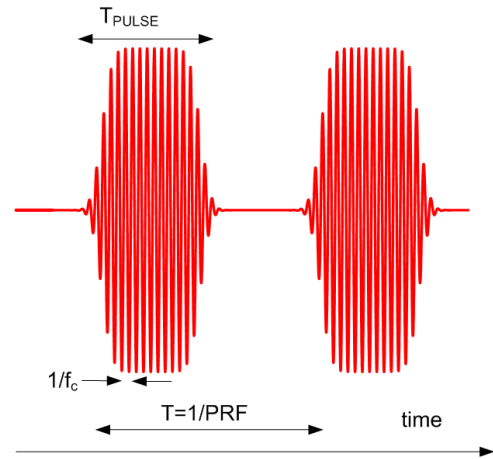


FIGURE 1. Schema of the transmitted radar waveforms.

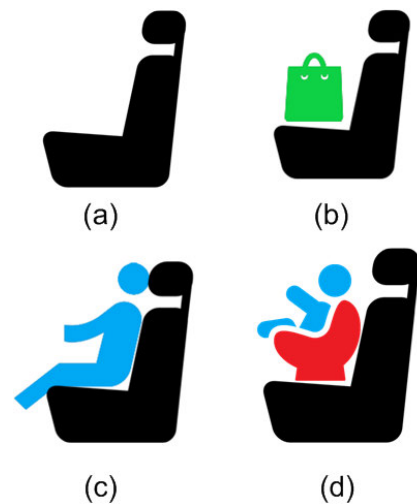


FIGURE 2. Seat states considered: (a) empty, (b) with a passive object, (c) adult, and (d) baby.

where $p(\tau)$ is the envelope of the wavelet and T is the inverse of the pulse repetition frequency (PRF). The signal received at the radar is the transmitted signal delayed and attenuated due to the propagation, plus the noise added by the receiver. The system relies on the fact that the pulses are transmitted with phase coherence. This makes it possible to reduce noise and improve the signal-to-noise ratio (SNR) in order to enhance the target detection, by combining the received signal from multiple transmitted phase coherent pulses [45]. The envelope is the module of the in-phase and quadrature demodulated signals (IQ) on the radar. After the coherent integration of the transmitted pulses, the envelope of the received signal can be expressed as a function of the delay τ for each sweep time t , and can be modeled as follows:

$$x_r(\tau, t) = \alpha \cdot p(\tau - \tau_0) + n(t) \tag{3}$$

where α is an attenuation term that depends on the distance and the reflection coefficient of the body and τ_0 is the delay due to round-trip between the target and the radar, and $n(t)$ is

the noise signal in the receiver. The radar module considers that there is a target if the amplitude of the envelope exceeds a certain threshold value. This threshold value can be configured to be a fixed value, or it can be estimated using a cell averaging constant false alarm (CA-CFAR) algorithm [45]. In this work, a constant threshold is considered, and it is determined from a measurement with the radar pointing to an empty seat.

The distance between the body and the radar can be modeled as the sum of the average distance r_0 and two terms that take into account the periodic movement of the chest, with maximum displacement r_b , and the random movements of the body induced by the car vibrations ($r_v(t)$):

$$r(t) = r_0 + r_b \cos(2\pi f_b t) + r_v(t) \quad (4)$$

In this model, the movement induced by the heartbeat is not considered because it is assumed to be masked by the breathing movement and the vibration of the car. With the car in motion, the randomness and changes in the road surface are the main factors that cause vibrations in a vehicle [46]. It can be used to analyze the influence of vehicle structural parameters and road excitation on vehicle random vibration.

It has been proven that the coefficient of rolling resistance of the vehicle increases with increasing road roughness coefficient. On the other hand, the vehicular rolling resistance force is also affected by vehicle speed, due to deformation of the tread and vibration in the tire rim caused by increased speed. The power spectrum density (PSD) depends on the kind of vehicle and has a significant content within the band between 1 Hz and 100 Hz [47].

The distance (r_0) to the body can be estimated from the envelope peak τ_{peak} of the measured signal as a function of the delay, which is returned by the radar firmware using the envelope service provided by the radar manufacturer [48].

The amplitude of the peak $y(t) = x_r(\tau_{peak}, t)$ provides information about movement and breathing. The received pulse waveform can be developed in a Taylor series assuming that the amplitude of the displacement due to breathing and random vibrations is small compared to the mean distance.

$$y(t) = x_r(\tau_{peak}, t) = A \cdot \sum_{n=0}^{\infty} \frac{p^{(n)}(0)}{n!} (\tau_b \cos(2\pi f_b t) + \tau_v(t))^n + n(t) \quad (5)$$

where $\tau_b = 2d_b/c$ and $\tau_v = 2d_v/c$ are the maximum delays associated with the breathing movement and vibration, respectively, being d_b the micromovement of the chest due to breathing and d_v the random micromovement due to vibration. t is the slow-time corresponding to the each radar sweep $t = nT_s$, where T_s is the time between each radar sweep. The amplitude A depends on the distance between the radar and the target and on its radar cross section.

The micromovements of the chest due to breathing and random movements of the body produce an envelope modulation as a function of slow time. The interference due to

random movements can be appreciated in (5). The fundamental harmonic of the breathing frequency corresponds to the term $n = 1$. The spectrum can be filtered to avoid important frequency interference, but if the amount of random movements is high, the interference occurs within the frequency range of the breathing (from 0.1 Hz to 1 Hz). Additionally, intermodulation products can also fall within the breathing spectrum.

B. SIGNAL PROCESSING

1) SEAT OCCUPANCY DETECTION

In absence of an occupant, the distance detected by the radar corresponds to the distance to the seat or any object located on the seat (eg. a bag). Therefore, it remains constant if the target is assumed to be static. In this case, small variations are due to noise and vibrations. In order to determine the presence of a person, the standard deviation of the AC component of the envelope amplitude is computed:

$$\sigma^2(t) = \int_0^t \left(\frac{dy}{dt} \right)^2 dt \quad (6)$$

A digital implementation of (6) is possible from the samples of the measured peak amplitude $y[n]$ returned by the radar in each sweep. To perform its implementation on micro-controllers with low memory resources, low-pass filters based on exponentially weighted moving average (EWMA) are used. This moving average filter is equivalent to an infinite impulse response (IIR) filter. This filter has the advantage that it is not necessary to save samples previously, only having to easily fit one coefficient or parameter. Using an EWMA filter, equation (6) can be implemented as follows:

$$\sigma^2[n] = \alpha \left(\frac{y[n] - y[n-1]}{T_s} \right)^2 + (1 - \alpha)\sigma^2[n-1] \quad (7)$$

where the derivative is approximated by the finite difference between two consecutive samples. The parameter α is the smoothing coefficient that can be obtained from the cut-off frequency [49]:

$$\alpha = \sqrt{\cos^2(\Omega_{3dB}) - 4 \cos(\Omega_{3dB}) + 3 + \cos(\Omega_{3dB})} - 1 \quad (8)$$

where Ω_{3dB} is the normalized angular frequency:

$$\Omega_{3dB} = f_c \frac{T_s}{2\pi} \quad (9)$$

The seat is considered to be occupied by a human if σ is higher than a threshold σ_{th} . Fig. 3 shows a block diagram of the signal processing used to obtain the seat occupancy. For the case of a stationary target the finite difference between consecutive samples must be zero and only noise contribution should be present. Consequently, σ will be an estimation of the noise deviation. The threshold is initially estimated from the average value of σ when the seat is empty. An excessively small value increases the probability of false alarm, while a high value can cause detection errors or delays in the response of the presence sensor. We have assessed that the noise level remains almost constant if the radar settings do not change.

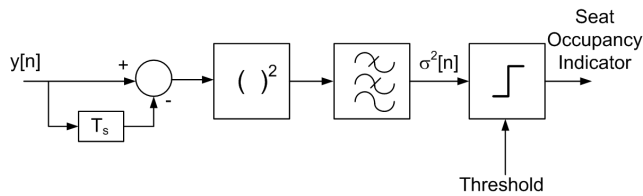


FIGURE 3. Block diagram of the signal processing used to obtain the seat occupancy.

2) BREATHING RATE DETERMINATION

In order to obtain the breathing rate, signal processing has been carried out. Firstly, a band pass filter between 0.1 Hz and 1 Hz has been applied to the amplitude of the envelope $y(t)$. Breathing signal is obtained by applying a band pass filter to the amplitude of the envelope $y(t)$. To avoid the use of high order filters that can introduce undesired delays, the band-pass filter is implemented in two steps. Firstly, the DC component is removed from the signal and then a low-pass filter is applied to remove components outside the breathing spectrum. In order to detect the variations produced by the movement of the body, a low-pass filter with a very low cut-off frequency (less than 0.1 Hz) is used. In absence of body movements and car vibrations the resulting signal $b(t)$ should be composed by the fundamental and the first harmonics of the breathing signal.

$$y_{DC}(t) = h_1(t) * y(t) \tag{10}$$

$$b(t) = h_2(t) * (y(t) - y_{DC}(t)) \tag{11}$$

where the symbol $*$ denotes the convolution operator and $h_1(t)$ and $h_2(t)$ are the impulsional response of the low-pass filters used to estimate the DC component and removing high frequency noise and components from $y(t)$, respectively. The practical implementation of these digital filters is described below.

Considering the possibility of performing the real-time implementation in a low-power microcontroller, the filter to remove the DC component h_1 can be implemented with an EWMA filter:

$$y_{DC}[n] = \alpha_1 y[n] + (1 - \alpha_1) y_{DC}[n - 1] \tag{12}$$

To perform the low pass filter h_2 there are several options [50], [51]. IIR filters provide higher attenuation with a lower order than FIR filters. In order to save memory a cascaded biquadratic filter has been used, whose transfer function is given by [52]:

$$H_2(z) = \frac{B(z)}{X(z)} = \frac{b_0 + b_1 z^{-1} + b_2 z^{-2}}{1 + a_1 z^{-1} + a_2 z^{-2}} \tag{13}$$

This filter can be implemented in a relatively simple difference-equation form, also known as Direct Form I, which can be easily applied to a time-based data stream:

$$b[n] = b_0 x[n] + b_1 x[n - 1] + b_2 x[n - 2] - a_1 b[n - 1] - a_2 b[n - 2] \tag{14}$$

where the input sequence $x[n]$ (see Fig. 4) is the breathing signal $y[n]$ after removing the DC component:

$$x[n] = y[n] - y_{DC}[n] \tag{15}$$

Alternatively, direct form II implementation can be used, which requires only two delay registers. To increase the attenuation, the filter can be applied in cascade to $b[n]$. The biquadratic filter coefficients (a_n and b_n) can be obtained from the desired corner frequency and quality factor [53].

In order to determine the body movements, the deviation of the distance σ_d can be computed by replacing the amplitude samples $y[n]$ by the distance samples $d[n]$ in (7).

Vital signs monitoring systems are often focused on determining the heart and breathing rates. At this point, the breathing rate can be determined from the filtered sequence $b[n]$. It can be obtained from the spectrum by applying a finite time window. However, this approach has some drawbacks. The most important one is that Fourier transforms are required, therefore it is necessary to save long data sequences that involve a great computational effort, especially if it has to be implemented in a low-power microcontroller. On the other hand, some physiological events, such as apneas, are detected from the reduction of the breathing rate and its duration is difficult to assess. The breathing rate is calculated from the average of the signal measured within the time window. Therefore, the respiration rate variability (RRV), which is obtained from the measurement of the changes in the time interval between breaths cannot be analyzed. Random body movements within the time window used to estimate the spectrum produce peaks in the spectrum that can be erroneously considered as breathing components. Some of these drawbacks can be overcome if the breathing signal is analyzed in the time domain.

To this end, a peak search algorithm is used to determine the breathing interval between two breaths. The algorithm described in [54] [55] is employed. It is based on searching a maximum (or minimum) The algorithm does not start another search until the trend of the signal has reversed (decreases after a maximum or increases after a minimum) the value specified by a parameter Δ . A suitable large enough value for this parameter provides a very robust behavior against noise. In addition, nearby peaks that produce impossible breathing frequencies are discarded. In order to amplify the breathing contribution, a nonlinear transformation is applied to compress the signal between two limits:

$$b_n[n] = \tanh\left(\frac{b[n]}{\sqrt{2}\sigma_b}\right) \tag{16}$$

where σ_b is the standard deviation of the breathing signal. Fig. 4 shows the main blocks diagrams used for the breathing rate calculation.

IV. EXPERIMENTAL VALIDATION

Several experiments have been conducted to show to feasibility of the system. The radar has been located facing the driver's seat (see Fig. 5) and the algorithm presented above

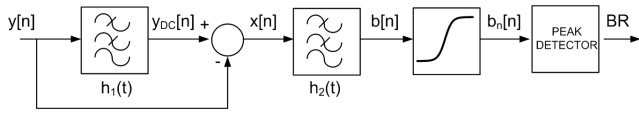


FIGURE 4. Block diagram of the signal processing used to obtain the breathing rate.



FIGURE 5. Image of the radar installer in the car oriented to the driver.

has been applied. The acquisition range of the radar is set typically between 0.5 m and 1 m. Therefore, any reflection that occurs outside of this range limit is ignored.

A. SEAT OCCUPANCY

Fig. 6 shows the results corresponding to the first situation (case 1) that has been measured. In this case, the seat remains empty (Fig. 2a) for 30 seconds, then a passenger enters, leaves a bag (Fig. 2.b) and exits the car. It can be seen that while the seat is empty or occupied by an object, the range of the maximum detected (Fig. 6a) and the peak amplitude ((Fig. 6b) remain constant. The time interval in which the passenger is in the seat produces a variation of the peak amplitude. During this interval the deviation σ increases and exceeds the threshold that activates the seat occupancy indicator (shown in dotted line in the Fig. 6c). During this interval breathing rate can be detected (Fig. 6d).

Fig. 7 shows the results corresponding to a second situation (case 2). Here the measurement begins with the engine switched off and the person occupying the driver’s seat. After 30 seconds the driver gets out of the car and re-enters after approximately 30 seconds. Then the driver starts the engine and after 50 seconds he stops it and exits the car. Both the range and the amplitude are nearly constant when the seat is empty and the deviation is below the threshold, which is set at the same value as in case 1.

B. BREATHING RATE RESULTS

This section compares the breathing rate measured with an air-flow sensor and with the radar. The air-flow temperature sensor consists of a negative temperature controlled (NTC) thermistor installed in a face mask (see Fig. 8). During the exhalation and inhalation process, the temperature rises

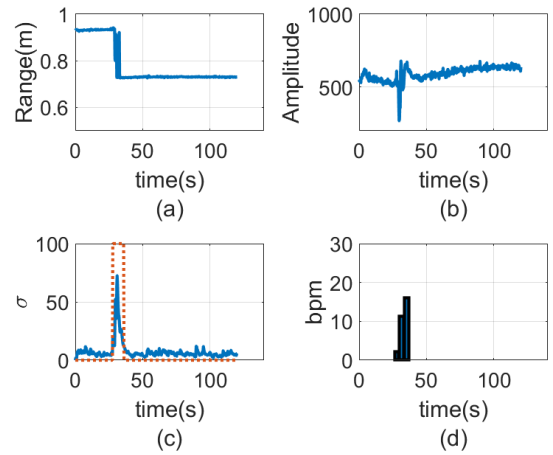


FIGURE 6. Case 1: (a) range, (b) amplitude, (c) deviation and seat occupancy indicator (dotted line), and (d) breathing rate.

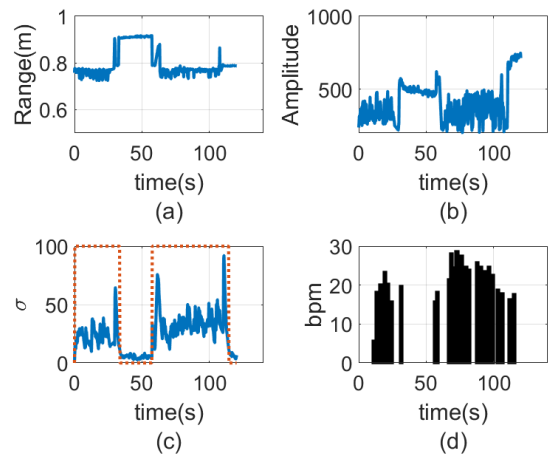


FIGURE 7. Case 2: (a) range, (b) amplitude, (c) deviation and seat occupancy indicator (dotted line), and (d) breathing rate.

and falls, respectively, as shown in Fig. 8. This temperature variation produces changes in the resistance of the NTC thermistor. The NTC used in this work is the G10K3976, whose nominal value is 10 kΩ at a temperature of 25°C. A Wheatstone resistive bridge connected an operational amplifier (LMV358 from Texas Instruments) is used to amplify the sensed signal (see Fig. 9). The output of the amplifier is digitized with the ESP32 microcontroller from Espressif, which integrates a 12-bit analog-to-digital converter (ADC). The same signal processing algorithm explained in section III-B is applied to both sensors.

To perform the comparison between both sensors, a person is seated stationary in front of the radar with the air-flow temperature sensor adjusted to the face using a mask. The measurements have been made with volunteers sitting still in order to avoid interference measured on the radar or in the position of the air flow sensor due to movement, which could produce outliers. The effect of random body movements will be studied later. An example of these measurements is

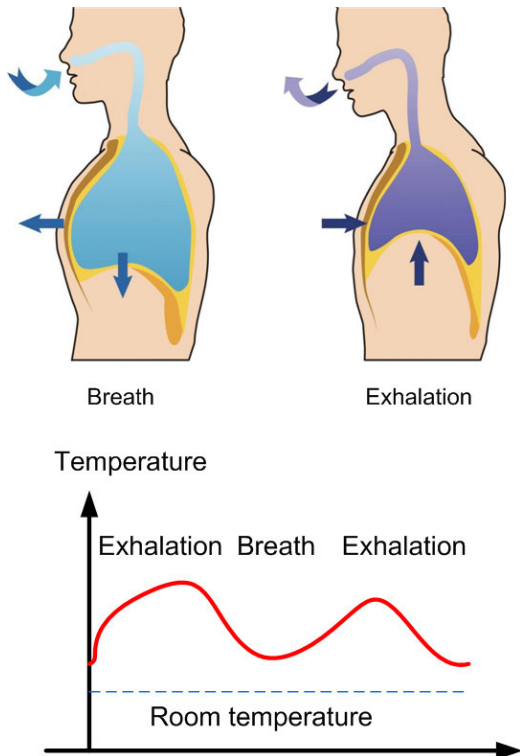


FIGURE 8. Air flow sensor based on sensing the variation of temperature measured with a thermistor.

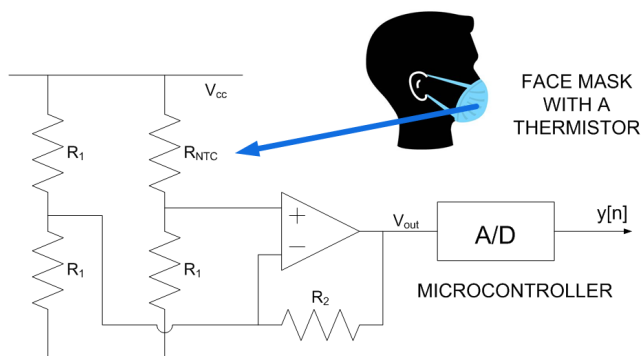


FIGURE 9. Signal conditioning used for air flow sensor.

shown in Fig. 10. This figure shows the radar $b[n]$ and the air-flow output signal recorded for 3 minutes. Good agreement between both sensors can be observed. Fig. 11 compares the breathing rate obtained from the two sensors.

A Bland–Altman plot (difference plot) is a data plotting method used to analyze the agreement between two different trials [56], [57]. It consists in plotting the difference between the two methods as a function of the average measurement. Bland–Altman analysis of Fig. 12 shows that the result does not depend on the proportional error. However, it does depend on the magnitude of the measurements. The Bland–Altman analysis reveals a bias of 0.2 bpm and a confidence range of 2.4 and -1.93 bpm. The analyses have been repeated with several volunteers achieving similar results.

The effect of random body movements in determining the breathing rate is studied in the next figures. To this end

and accelerometer is connected to a microcontroller via an I2C bus. The accelerometer is placed around the chest with the help of a ribbon. Both the acceleration and the radar signal are recorded simultaneously. A measurement is shown in Fig. 13. Fig. 14 shows both the normal component of acceleration due to the chest movement and the spectrogram. A periodic change associated with breathing movements can be observed, resulting in an almost constant peak in frequency as a function of time. However, random movements around 30 and 50 seconds produce a strong interference in all the spectrum making difficult the measurement of the breathing rate. Under these circumstances, there is a rapid variation of the signal in the time domain. Consequently, a small interval appears between adjacent peaks, causing an erroneous estimation of the breathing rate. Since the breathing rate is computed from the inverse of the breathing interval, these periods do not affect the estimation of the breathing rate of the next interval. These abnormally high values do not represent any inconvenience, since they can be easily detected and neglected. The seat occupancy indicator works

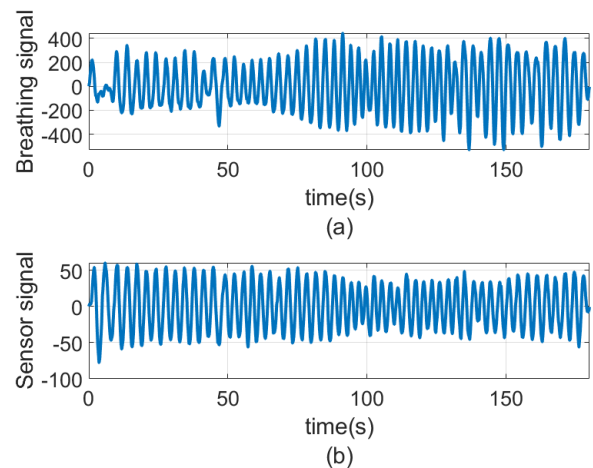


FIGURE 10. Breathing signal from the radar (a) and for air flow sensor (b).

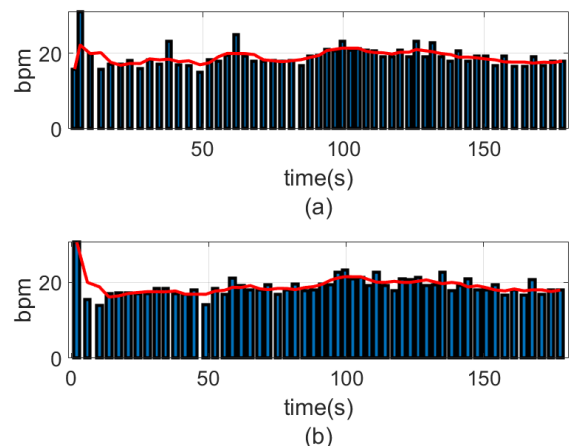


FIGURE 11. Breathing rate as a function of the time obtained from the radar (a) and the air flow sensor (b).

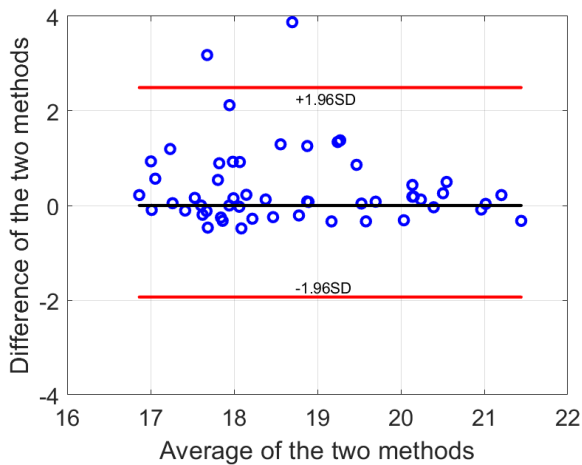


FIGURE 12. Bland-Altman plot for the breathing rate.

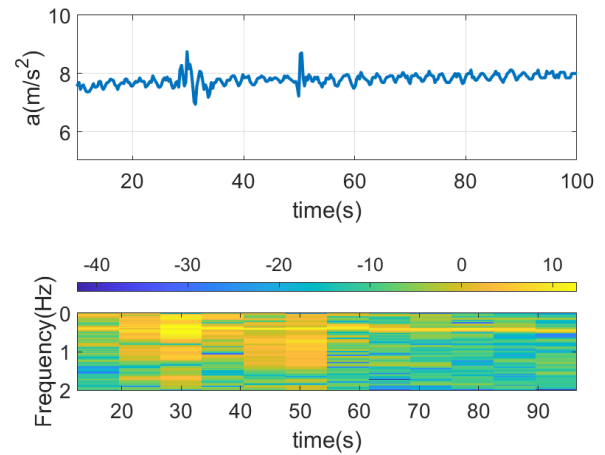


FIGURE 14. Measured chest acceleration (top) and spectrogram (bottom).

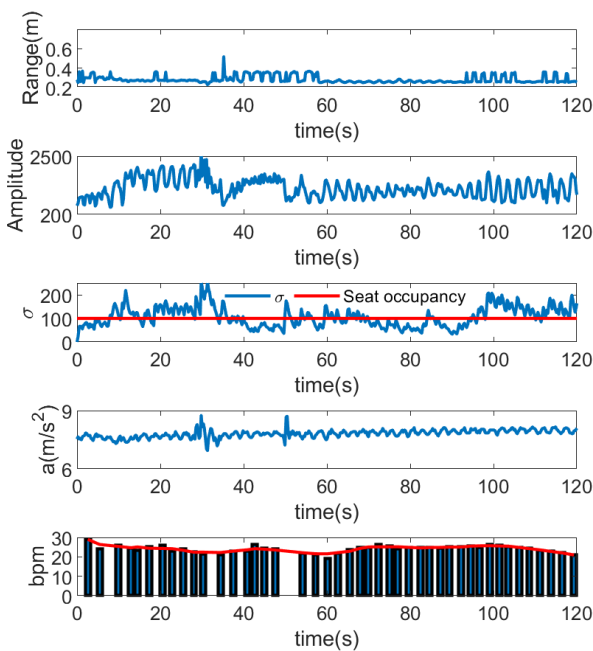


FIGURE 13. From top to bottom: measured peak distance, amplitude, standard deviation, chest acceleration and breathing rate including reference airflow sensor (red line).

correctly over the entire time interval of the measurement because the envelope deviation σ is higher than the threshold. It is observed that the values of σ increase for the period of random body movements. In order to reduce the interference of movements of the arms that can block the line-of-sight of the radar, the radar could be integrated into the roof of the car, to have direct visibility of the subject's chest. Another improvement would be the use of lens antennas to increase their directivity, thus reducing the interference from surrounding objects. Reflections that fall outside the range window determined by the time-gating interval are considered to be ignored. Therefore, interference from movements of passengers is eliminated.

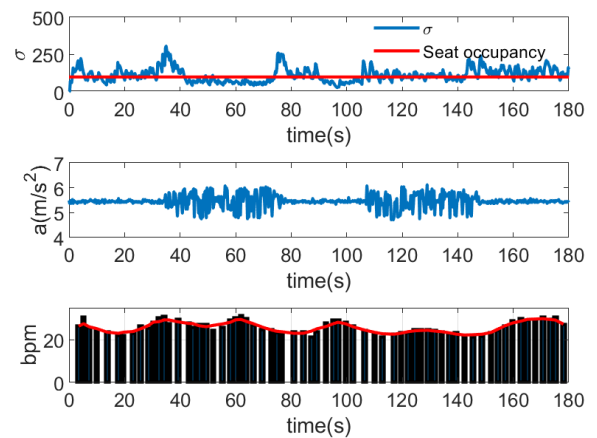


FIGURE 15. Influence of car vibrations. From top to bottom: standard deviation, normal radar acceleration and breathing rate including reference airflow sensor (red line).

The influence of car vibrations both at rest and in motion is studied in the following figures. To this end, an accelerometer is attached to the radar support to measure the acceleration suffered by the radar. The acceleration is simultaneously recorded with the radar measurements using a microcontroller connected to a computer. An example of measurement is shown in Fig. 15. The engine is initially stopped. After 35 seconds, the driver starts the car engine, and after another 25 seconds, he stops it. The procedure is repeated again. Fig. 16 shows the spectrogram of the acceleration. Fig. 17 shows the breathing rate variability in a Poincare plot. This plot shows the scatter obtained from the correlation between two consecutive data points in a time series. It consists in a scatter plot of the current breathing duration plotted against the previous breathing interval. SD1 and SD2 (standard deviations outside and inside the axis, respectively) are approximately the same with both the engine off and on. It can be shown that the effect of the car vibrations is small because the high frequency components are filtered out.

Now the system has been tested in a real environment. An urban scenario has been chosen where the driver must

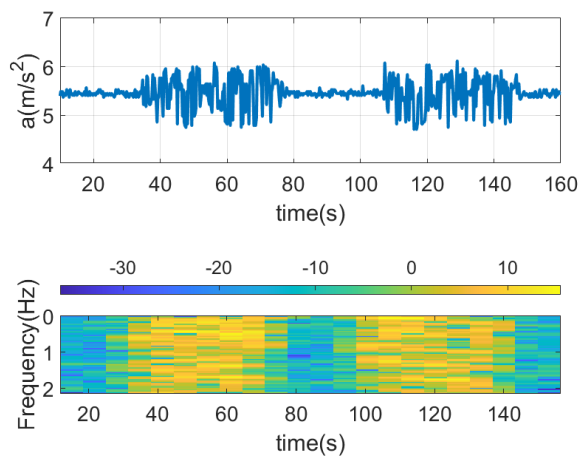


FIGURE 16. Measured radar acceleration (top) and spectrogram (bottom) with the engine off and on.

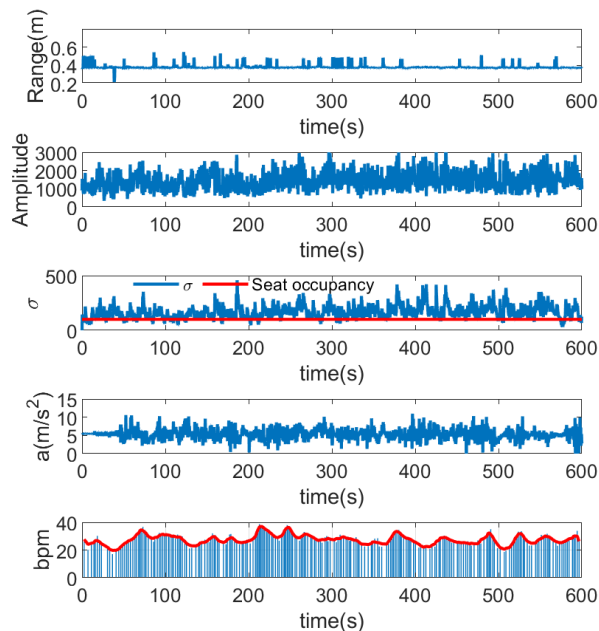


FIGURE 18. Measurements in an urban travel of 10 min. From top to bottom: measured peak distance, amplitude, standard deviation, chest acceleration and breathing rate including reference airflow sensor (red line).

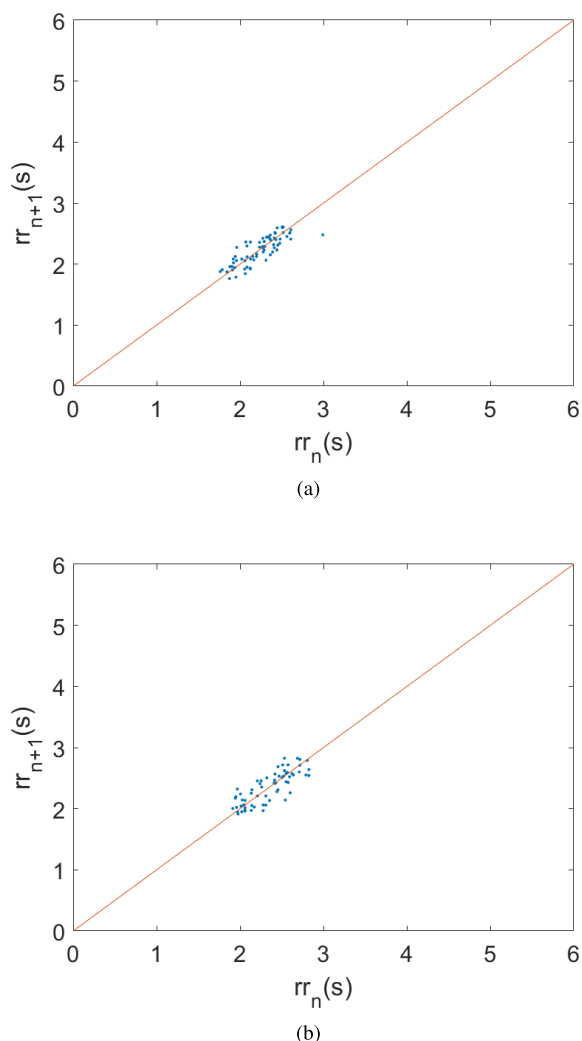


FIGURE 17. Poincare analysis: (a) engine off, (b) engine on.

move the steering wheel sharply and accelerate and brake repeatedly along the way. Fig. 18 shows the measured results

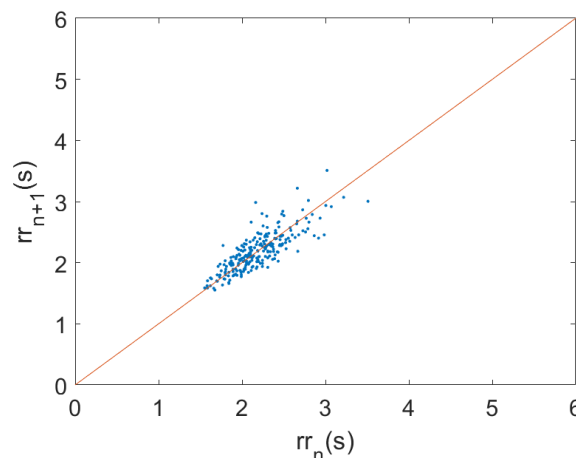


FIGURE 19. Poincare analysis for a travel of 10 min.

caused by the driver breathing activity. Fig. 19 shows the Poincare plot for a driver measured during this travel. Due to the activity of the driver, the breathing variability increases with respect to the situations corresponding to periods of rest. An increase of outliers has not been observed during the trips, this fact shows the robustness of the proposed framework. It shows the potential feasibility of the system to study the driver’s drowsiness and stress [58] based on the variability of the breathing rate. To this end, parameters such as the average breathing rate and the standard deviation of the distances of points located both off the axis of the bisector and along the axis, SD1 and SD2 [59], can be tracked as a function of time.

Fig. 20 and Fig. 21 show the Poincare plot and the breathing rate as a function of the time obtained during a travel

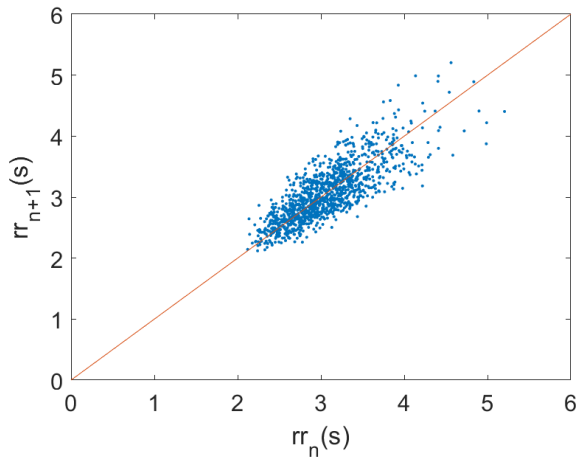


FIGURE 20. Poincare analysis for a travel in the highway of 1h.

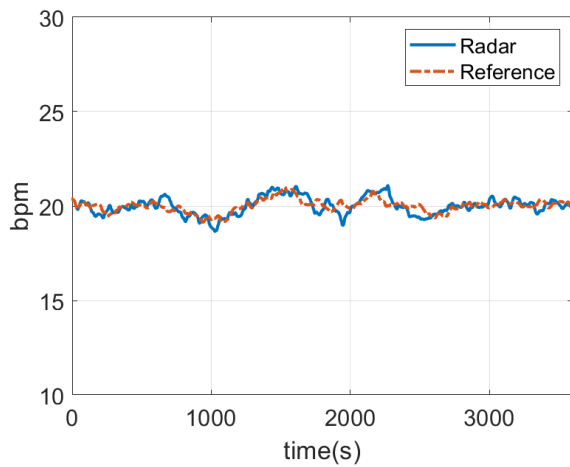


FIGURE 21. Breathing rate as a function of the time for a travel in the highway of 1 h determined by the radar and the reference sensor (dashed line).



FIGURE 22. Photography of baby emulator in a seat with an electromechanical transducer.

by a highway of an hour of duration. We can observe that the breathing rate is slightly lower and trend to be almost constant that can indicate low a driver activity and symptoms of a certain degree of drowsiness.

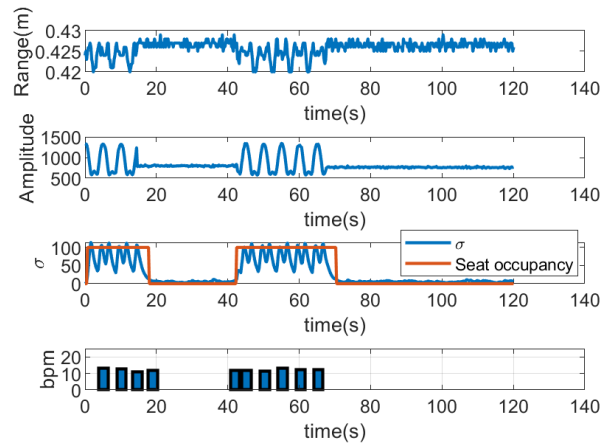


FIGURE 23. Measurement with a baby seat emulator: from top to bottom: measured peak distance, amplitude, standard deviation, and breathing rate.

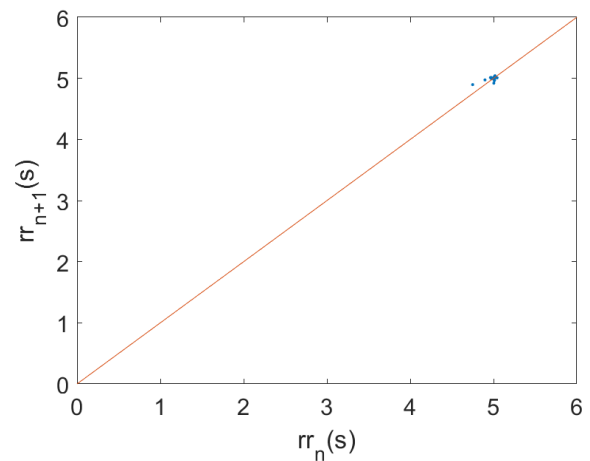


FIGURE 24. Poincare analysis for a baby emulator at 12 bpm (0.2 Hz).

C. BABY SEAT DETECTION

To study the seat occupancy detection for the case of a baby with a child seat (Fig. 2d), an emulator has been designed. An electromechanical transducer (a loudspeaker) connected to a low-frequency generator has been used to simulate the movements of the baby’s chest. Fig. 22 shows a photograph of the emulator installed in a car seat. Fig. 23 shows a measurement with the emulator moving at a frequency of 0.2 Hz (12 bpm). The generator is turned on and off to simulate the seat occupancy. Results show that the system can detect the movements of the transducer, thus raising an indicator that the seat is occupied when the generator is enabled. Fig. 24 shows the Poincare plot when the generator is continuously enabled at 0.2 Hz which corresponds to a period of 5 s. Similar results have been obtained at other frequencies from 0.1 Hz to 1 Hz.

V. CONCLUSION AND FUTURE WORK

A seat occupancy detection system based on an integrated PCR (Pulse Coherent Radar) technology at the unlicensed 60 GHz ISM frequency band, has been investigated. The radar

can measure distance with sub-millimeter resolution, allowing to distinguish small body movements, which are used to detect the presence of persons. A detector based on the estimation of the standard deviation of the peak amplitude differences and a threshold comparator has been proposed. Therefore, the system can distinguish the presence of a human being from other objects that can occupy the seat.

Due to its high resolution, it is possible to measure the breathing rate from the changes in the peak amplitude. To this end, digital filters to remove the DC component and noise are applied. The measurement of the breathing rate is performed from the time interval between two peaks associated with breathing. This method does not require computational charge compared with other methods based on spectrum estimation and, therefore, can be implemented on low-power microcontrollers. The influence of random body movements and vibrations in the measurement of the breathing rate has been investigated. Body movement produces an interference that blocks the correct estimation of the breathing cycles. Random movements associated to car vibrations are treated as broadband noise. Therefore, it is filtered by the digital filter and the effect is small. Bland–Altman analysis have been performed to compare the radar measurements with an air-flow sensor, obtaining mean differences less than 2 bpm. The system has been tested in an urban circuit to measure the breathing of the driver showing its potential use to monitor the drowsiness state or driver fatigue. A baby emulator has also been used to show the possibility to detect child seat occupancy. Another potential use of the system could be the monitoring of apneas and the study of sleep quality.

REFERENCES

- J. W. Melvin, "Injury assessment reference values for the CRABI 6-month infant dummy in a rear-facing infant restraint with airbag deployment," in *Proc. SAE Tech. Paper Ser.*, Feb. 1995, pp. 1553–1564.
- A. R. Diewald, J. Landwehr, D. Tatarinov, P. D. M. Cola, C. Watgen, C. Mica, M. Lu-Dac, P. Larsen, O. Gomez, and T. Goniva, "RF-based child occupation detection in the vehicle interior," in *Proc. 17th Int. Radar Symp. (IRS)*, May 2016, pp. 1–4.
- P. Napoletano and S. Rossi, "Combining heart and breathing rate for car driver stress recognition," in *Proc. IEEE 8th Int. Conf. Consum. Electron. Berlin (ICCE-Berlin)*, Sep. 2018, pp. 1–5.
- L. Findley, C. Smith, J. Hooper, M. Dineen, and P. M. Suratt, "Treatment with nasal CPAP decreases automobile accidents in patients with sleep apnea," *Amer. J. Respiratory Crit. Care Med.*, vol. 161, no. 3, pp. 857–859, Mar. 2000.
- I. Gurubhagavatula, G. Maislin, J. E. Nkwuo, and A. I. Pack, "Occupational screening for obstructive sleep apnea in commercial drivers," *Amer. J. Respiratory Crit. Care Med.*, vol. 170, no. 4, pp. 371–376, Aug. 2004.
- M. M. Lyons, J. F. Kraemer, R. Dhingra, B. T. Keenan, N. Wessel, M. Glos, T. Penzel, and I. Gurubhagavatula, "Screening for obstructive sleep apnea in commercial drivers using EKG-derived respiratory power index," *J. Clin. Sleep Med.*, vol. 15, no. 1, pp. 23–32, Jan. 2019.
- N. Rodríguez-Ibañez, M. A. García-González, M. A. F. de la Cruz, M. Fernández-Chimeno, and J. Ramos-Castro, "Changes in heart rate variability indexes due to drowsiness in professional drivers measured in a real environment," in *Proc. Comput. Cardiol.*, Sep. 2012, pp. 913–916.
- S. D. Da Cruz, H.-P. Beise, U. Schroder, and U. Karahasanovic, "A theoretical investigation of the detection of vital signs in presence of car vibrations and RADAR-based passenger classification," *IEEE Trans. Veh. Technol.*, vol. 68, no. 4, pp. 3374–3385, Apr. 2019.
- A. Voisin, S. Bombardier, E. Levrat, and J. Bremont, "Sensory features measurement of the under-thigh length of car seat," in *Proc. IEEE Int. Conf. Fuzzy Syst. IEEE World Congr. Comput. Intell.*, vol. 2, May 1998, pp. 1589–1594.
- K. Kasten, A. Stratmann, M. Munz, K. Dirscherl, and S. Lamers, "iBolt technology—A weight sensing system for advanced passenger safety," in *Advanced Microsystems for Automotive Applications*. Berlin, Germany: Springer, 2006, pp. 171–186.
- B. George, H. Zangl, T. Bretterkieber, and G. Brasseur, "Seat occupancy detection based on capacitive sensing," *IEEE Trans. Instrum. Meas.*, vol. 58, no. 5, pp. 1487–1494, May 2009.
- D. Tumpold and A. Satz, "Contactless seat occupation detection system based on electric field sensing," in *Proc. 35th Annu. Conf. IEEE Ind. Electron.*, Nov. 2009, pp. 1823–1828.
- M. Walter, B. Eilebrecht, T. Wartzek, and S. Leonhardt, "The smart car seat: Personalized monitoring of vital signs in automotive applications," *Pers. Ubiquitous Comput.*, vol. 15, no. 7, pp. 707–715, Oct. 2011.
- M. Fritzsche, C. P. G. Becker, M. Castillo-Franco, and B. Mirbach, "Vehicle occupancy monitoring with optical range-sensors," in *Proc. IEEE Intell. Vehicles Symp.*, Jun. 2004, pp. 90–94.
- M. Mateu-Mateus, F. Guede-Fernández, N. Rodríguez-Ibáñez, M. A. García-González, J. Ramos-Castro, and M. Fernández-Chimeno, "A non-contact camera-based method for respiratory rhythm extraction," *Biomed. Signal Process. Control*, vol. 66, Apr. 2021, Art. no. 102443.
- A. Lazaro, D. Girbau, and R. Villarino, "Analysis of vital signs monitoring using an IR-UWB radar," *Prog. Electromagn. Res.*, vol. 100, pp. 265–284, 2010.
- A. Lazaro, D. Girbau, and R. Villarino, "Techniques for clutter suppression in the presence of body movements during the detection of respiratory activity through UWB radars," *Sensors*, vol. 14, no. 2, pp. 2595–2618, 2014.
- F. Khan and S. H. Cho, "A detailed algorithm for vital sign monitoring of a stationary/non-stationary human through IR-UWB radar," *Sensors*, vol. 17, no. 2, p. 290, 2017.
- W. H. Lee, Y. Lee, J. Y. Na, S. H. Kim, H. J. Lee, Y.-H. Lim, S. H. Cho, S. H. Cho, and H.-K. Park, "Feasibility of non-contact cardiorespiratory monitoring using impulse-radio ultra-wideband radar in the neonatal intensive care unit," *PLoS ONE*, vol. 15, no. 12, Dec. 2020, Art. no. e0243939.
- C. Li, J. Cummings, J. Lam, E. Graves, and W. Wu, "Radar remote monitoring of vital signs," *IEEE Microw. Mag.*, vol. 10, no. 1, pp. 47–56, Feb. 2009.
- D. Girbau, A. M. Roldan, A. Ramos, and R. Villarino, "Remote sensing of vital signs using a Doppler radar and diversity to overcome null detection," *IEEE Sensors J.*, vol. 12, no. 3, pp. 512–518, Mar. 2012.
- C. Li, V. M. Lubecke, O. Boric-Lubecke, and J. Lin, "A review on recent advances in Doppler radar sensors for noncontact healthcare monitoring," *IEEE Trans. Microw. Theory Techn.*, vol. 61, no. 5, pp. 2046–2060, May 2013.
- Y. Iwata, H. T. Thanh, G. Sun, and K. Ishibashi, "High accuracy heartbeat detection from CW-Doppler radar using singular value decomposition and matched filter," *Sensors*, vol. 21, no. 11, p. 3588, May 2021.
- H. Lee, B.-H. Kim, J.-K. Park, and J.-G. Yook, "A novel vital-sign sensing algorithm for multiple subjects based on 24-GHz FMCW Doppler radar," *Remote Sens.*, vol. 11, no. 10, p. 1237, 2019.
- Y. Wang, W. Wang, M. Zhou, A. Ren, and Z. Tian, "Remote monitoring of human vital signs based on 77-GHz mm-wave FMCW radar," *Sensors*, vol. 20, no. 10, p. 2999, May 2020.
- Z. Yang, P. H. Pathak, Y. Zeng, X. Liran, and P. Mohapatra, "Monitoring vital signs using millimeter wave," in *Proc. 17th ACM Int. Symp. Mobile Ad Hoc Netw. Comput.*, Jul. 2016, pp. 211–220.
- T. Zhang, J. Sarrazin, G. Valerio, and D. Istrate, "Estimation of human body vital signs based on 60 GHz Doppler radar using a bound-constrained optimization algorithm," *Sensors*, vol. 18, no. 7, p. 2254, Jul. 2018.
- H.-C. Kuo, C.-C. Lin, C.-H. Yu, P.-H. Lo, J.-Y. Lyu, C.-C. Chou, and H.-R. Chuang, "A fully integrated 60-GHz CMOS direct-conversion Doppler radar RF sensor with clutter canceller for single-antenna noncontact human vital-signs detection," *IEEE Trans. Microw. Theory Techn.*, vol. 64, no. 4, pp. 1018–1028, Apr. 2016.
- H.-I. Choi, W.-J. Song, H. Song, and H.-C. Shin, "Selecting target range with accurate vital sign using spatial phase coherency of FMCW radar," *Appl. Sci.*, vol. 11, no. 10, p. 4514, May 2021.
- Q. Wu, Z. Mei, Z. Lai, D. Li, and D. Zhao, "A non-contact vital signs detection in a multi-channel 77GHz LFM CW radar system," *IEEE Access*, vol. 9, pp. 49614–49628, 2021.
- G. Vinci, T. Lenhard, C. Will, and A. Koelpin, "Microwave interferometer radar-based vital sign detection for driver monitoring syst," in *IEEE MTT-S Int. Microw. Symp. Dig.*, Apr. 2015, pp. 1–4.

- [32] S. K. Leem, F. Khan, and S. H. Cho, "Vital sign monitoring and mobile phone usage detection using IR-UWB radar for intended use in car crash prevention," *Sensors*, vol. 17, no. 6, p. 1240, 2017.
- [33] S. Leonhardt, L. Leicht, and D. Teichmann, "Unobtrusive vital sign monitoring in automotive environments—A review," *Sensors*, vol. 18, no. 9, p. 3080, Sep. 2018.
- [34] M. Hoffmann, D. Tatarinov, J. Landwehr, and A. Diewald, "A four-channel radar system for rear seat occupancy detection in the 24 GHz ISM band," in *Proc. 11th German Microw. Conf. (GeMiC)*, Mar. 2018, pp. 95–98.
- [35] M. Alizadeh, H. Abedi, and G. Shaker, "Low-cost low-power in-vehicle occupant detection with mm-wave FMCW radar," in *Proc. IEEE Sensors*, Oct. 2019, pp. 1–4.
- [36] Y. Ma, Y. Zeng, and V. Jain, "CarOSense: Car occupancy sensing with the ultra-wideband keyless infrastructure," *Proc. ACM Interact., Mobile, Wearable Ubiquitous Technol.*, vol. 4, no. 3, pp. 1–28, Sep. 2020.
- [37] J. Yu, P. Wang, T. Koike-Akino, Y. Wang, P. V. Orlik, and H. Sun, "Human pose and seat occupancy classification with commercial MMWave WiFi," in *Proc. IEEE Globecom Workshops (GC Wkshps)*, Dec. 2020, pp. 1–6.
- [38] J. Weis and A. Santra, "Material classification using 60-GHz radar and deep convolutional neural network," in *Proc. Int. Radar Conf. (RADAR)*, Sep. 2019, pp. 1–6.
- [39] B. Ahmed, A. Kara, E. Zencir, and M. Benzaghta, "Opportunities and challenges in RCS measurement of 9-mm bullet model with 77 GHz mmwave COTS radar systems," *Microw. Opt. Technol. Lett.*, vol. 62, no. 12, pp. 3772–3778, Dec. 2020.
- [40] J. Bhatia, A. Dayal, A. Jha, S. K. Vishvakarma, J. Soumya, M. B. Srinivas, P. K. Yalavarthy, A. Kumar, V. Lalitha, S. Koorapati, and L. R. Cenkeramaddi, "Object classification technique for mmWave FMCW radars using range-FFT features," in *Proc. Int. Conf. Commun. Syst. Netw. (COM-SNETS)*, Jan. 2021, pp. 111–115.
- [41] J. B. Meister and B. L. Walcott, "Occupant and infant seat detection in a vehicle supplemental restraint system," U.S. Patent 5 570 903, Nov. 5, 1996.
- [42] M. Devy, A. Giralt, and A. Marin-Hernandez, "Detection and classification of passenger seat occupancy using stereovision," in *Proc. IEEE Intell. Vehicles Symp.*, Oct. 2000, pp. 714–719.
- [43] S. Wender and O. Loehlein, "A cascade detector approach applied to vehicle occupant monitoring with an omni-directional camera," in *Proc. IEEE Intell. Vehicles Symp.*, Jun. 2004, pp. 345–350.
- [44] *A111 Pulsed Coherent Radar (PCR)*, Acconeer AB, Stockholm, Sweden, Feb. 2021.
- [45] N. Levanon and E. Mozeson, *Radar Signals*. Hoboken, NJ, USA: Wiley, 2004.
- [46] A. Soliman, "Effect of road roughness on the vehicle ride comfort and rolling resistance," Warrendale, PA, USA, SAE Tech. Paper 2006-01-1297, 2006, doi: 10.4271/2006-01-1297.
- [47] K. Praznowski, J. Mamala, M. Śmieja, and M. Kupina, "Assessment of the road surface condition with longitudinal acceleration signal of the car body," *Sensors*, vol. 20, no. 21, p. 5987, Oct. 2020.
- [48] *Entry Module EVK Hardware User Guide-XE132*, Acconeer AB, Stockholm, Sweden, Sep. 2020.
- [49] D. Chaudhuri, M. Mukherjee, M. H. Khondekar, and K. Ghosh, "Simple exponential smoothing and its control parameter: A reassessment," in *Recent Trends in Signal and Image Processing*. Singapore: Springer, 2019, pp. 63–77.
- [50] J. G. Proakis, *Digital Signal Processing: Principles Algorithms and Applications*. London, U.K.: Pearson, 2001.
- [51] S. K. Mitra and Y. Kuo, *Digital Signal Processing: A Computer-Based Approach*, vol. 2. New York, NY, USA: McGraw-Hill, 2006.
- [52] M. D. Lutovac, D. V. Tošić, and B. L. Evans, *Filter Design for Signal Processing Using MATLAB and Mathematica*. Upper Saddle River, NJ, USA: Prentice-Hall, 2001.
- [53] C. Pradabpet, S. Yimman, W. Hinjit, S. Chivapreecha, and K. Dejhan, "Design and implementation of biquad digital filter," in *Proc. 9th Asia-Pacific Conf. Commun.*, Sep. 2003, pp. 1138–1142.
- [54] S. Milici, A. Lázaro, R. Villarino, D. Girbau, and M. Magnarosa, "Wireless wearable magnetometer-based sensor for sleep quality monitoring," *IEEE Sensors J.*, vol. 18, no. 5, pp. 2145–2152, Mar. 2018.
- [55] S. Milici, J. Lorenzo, A. Lázaro, R. Villarino, and D. Girbau, "Wireless breathing sensor based on wearable modulated frequency selective surface," *IEEE Sensors J.*, vol. 17, no. 5, pp. 1285–1292, Mar. 2017.
- [56] J. M. Bland and D. G. Altman, "Statistical methods for assessing agreement between two methods of clinical measurement," *Lancet*, vol. 327, no. 8476, pp. 307–310, Feb. 1986.
- [57] D. Giavarina, "Understanding bland Altman analysis," *Biochem. Med.*, vol. 25, pp. 141–151, Sep. 2015.
- [58] A. Hernando, J. Lazaro, E. Gil, A. Arza, J. M. Garzon, R. Lopez-Anton, C. de la Camara, P. Laguna, J. Aguilo, and R. Bailon, "Inclusion of respiratory frequency information in heart rate variability analysis for stress assessment," *IEEE J. Biomed. Health Informat.*, vol. 20, no. 4, pp. 1016–1025, Jul. 2016.
- [59] A. K. Golińska, "Poincaré plots in analysis of selected biomedical signals," *Stud. Log., Grammar Rhetoric*, vol. 35, no. 1, pp. 117–127, Dec. 2013.



ANTONIO LAZARO (Senior Member, IEEE) was born in Lleida, Spain, in 1971. He received the M.S. and Ph.D. degrees in telecommunication engineering from the Universitat Politècnica de Catalunya (UPC), Barcelona, Spain, in 1994 and 1998, respectively. Then, he joined the Faculty of UPC, where he currently teaches a course on microwave circuits and antennas. Since July 2004, he has been a full time Professor with the Department of Electronic Engineering, Universitat Rovira i Virgili (URV), Tarragona, Spain. His research interests include microwave device modeling, on-wafer noise measurements, monolithic microwave integrated circuits (MMICs), low phase noise oscillators, MEMS, RFID, UWB, and microwave systems.



MARC LAZARO was born in Tarragona, Spain, in 1995. He received the B.S. degree in industrial electronics and automation engineering and the M.S. degree in electronic systems engineering and technology (METSE) from Rovira i Virgili University, Tarragona, in 2017 and 2018, respectively, where he is currently pursuing the Ph.D. degree with the Department of Electronics. Up until now, he has accumulated professional experience as a data acquisition engineer and an embedded systems developer. His research interests include semipassive RFID technologies based on backscattering communication and novel applications based on millimeter wave identification (MMID).



RAMON VILLARINO received the degree in telecommunications technical engineering from Ramon Llull University (URL), Barcelona, Spain, in 1994, and the degree in senior telecommunications engineering and the Ph.D. degree from the Universitat Politècnica de Catalunya (UPC), Barcelona, in 2000 and 2004, respectively. From 2005 to 2006, he was a Research Associate at the Technological Telecommunications Center of Catalonia (CTTC), Barcelona. He worked as a Researcher and an Assistant Professor at the Universitat Autònoma de Barcelona (UAB), from 2006 to 2008. Since January 2009, he has been a full-time Professor at Universitat Rovira i Virgili (URV), Tarragona, Spain. His research interests include radiometry, microwave devices, and systems based on UWB, RFIDs, and frequency selective structures using metamaterials (MM).



DAVID GIRBAU (Senior Member, IEEE) received the B.Sc. degree in telecommunication engineering, the master's degree in electronics engineering, and the Ph.D. degree in telecommunication from the Universitat Politècnica de Catalunya (UPC), Barcelona, Spain, in 1998, 2002, and 2006, respectively. From February 2001 to September 2007, he was a Research Assistant at UPC. From September 2005 to September 2007, he was a part-time Assistant Professor at Universitat Autònoma de Barcelona (UAB). Since October 2007, he has been a full-time Professor at Universitat Rovira i Virgili (URV), Tarragona, Spain. His research interests include microwave devices and systems, with an emphasis on UWB, RFIDs, RF-MEMS, and wireless sensors.

• • •